

Low-Profile and Low-Visual Impact Smart Electromagnetic Curved Passive Skins for Enhancing Connectivity in Urban Scenarios

Original

Low-Profile and Low-Visual Impact Smart Electromagnetic Curved Passive Skins for Enhancing Connectivity in Urban Scenarios / Freni, Angelo; Beccaria, Michele; Mazzinghi, Agnese; Massaccesi, Andrea; Pirinoli, Paola. - In: ELECTRONICS. - ISSN 2079-9292. - ELETTRONICO. - 12:21(2023). [[10.3390/electronics12214491](https://doi.org/10.3390/electronics12214491)]

Availability:

This version is available at: 11583/2984359 since: 2023-12-05T16:12:15Z

Publisher:

MDPI

Published

DOI:[10.3390/electronics12214491](https://doi.org/10.3390/electronics12214491)

Terms of use:

This article is made available under terms and conditions as specified in the corresponding bibliographic description in the repository

Publisher copyright

(Article begins on next page)

Article

Low-Profile and Low-Visual Impact Smart Electromagnetic Curved Passive Skins for Enhancing Connectivity in Urban Scenarios

Angelo Freni ^{1,*}, Michele Beccaria ², Agnese Mazzinghi ¹, Andrea Massaccesi ² and Paola Pirinoli ²

¹ Department of Information Engineering, University of Florence, 50139 Florence, Italy; agnese.mazzinghi@unifi.it

² Department of Electronics and Telecommunications, Politecnico di Torino, 10129 Turin, Italy; michele.beccaria@polito.it (M.B.); andrea.massaccesi@polito.it (A.M.); paola.pirinoli@polito.it (P.P.)

* Correspondence: angelo.freni@unifi.it

Abstract: This paper explores the possibility of integrating a smart electromagnetic skin into a street light or traffic light pole to enhance the coverage of a 5G base station operating in the millimeter-waves frequency band with the consequent improvement of the wireless network performance. Specifically, the electromagnetic characteristics of a curved smart electromagnetic skin, which can be easily integrated into a cylindrical radome enclosing the pole, have been analyzed and compared with those of a planar solution. Additionally, the coverage provided by a curved smart electromagnetic skin in a real urban scenario has been considered. The obtained results confirm that using a curved smart electromagnetic skin is both feasible and convenient from several points of view: it guarantees better performance than a planar configuration occupying the same volume, it is simpler to mount and it has a lower visual impact.

Keywords: smart electromagnetic skin; reflectarray; 5G antennas



Citation: Freni, A.; Beccaria, M.; Mazzinghi, A.; Massaccesi, A.; Pirinoli, P. Low-Profile and Low-Visual Impact Smart Electromagnetic Curved Passive Skins for Enhancing Connectivity in Urban Scenarios. *Electronics* **2023**, *12*, 4491. <https://doi.org/10.3390/electronics12214491>

Academic Editor: Dimitra I. Kaklamani

Received: 6 September 2023

Revised: 27 October 2023

Accepted: 29 October 2023

Published: 1 November 2023



Copyright: © 2023 by the authors. Licensee MDPI, Basel, Switzerland. This article is an open access article distributed under the terms and conditions of the Creative Commons Attribution (CC BY) license (<https://creativecommons.org/licenses/by/4.0/>).

1. Introduction

Communication systems of the fifth generation (5G), with much more functionality than those of the fourth generation, have now become a reality, and are nowadays being installed around the world. Although they offer significant improvements compared to the oldest systems, they will not be able to fulfill all the requirements needed by the intelligent and fully integrated automated systems that are going to emerge in the next ten years. The analysis of the requirements that the next-generation of wireless communication systems will have to meet for future applications identifies the need for a higher transmission speed and very low latency as critical aspects. While there are not yet precise standards, the ambitious goals identified by 5G and beyond wireless systems are the following: fast data transfer rates, corresponding to 1 TB per second download speed; wide bandwidth availability; better coverage; almost zero latency (close to 0.1 ms); increase in overall data traffic and connected users; reduced energy consumption; capability of connecting intelligence rather than objects through the use of Artificial Intelligence (see for instance [1–3]).

From preliminary studies, it emerges that using mm-waves or sub-THz frequency bands can be very promising since they would allow reaching an extremely high bandwidth, managing an ultra-high data rate, and providing quasi-negligible latency. On the other hand, mm-waves and sub-THz frequencies suffer from higher free space loss, higher building penetration loss, and strong interaction with obstacles (e.g., foliage attenuation, rain attenuation, etc.) along the propagation path. As a result, the coverage can be significantly deteriorated, if not completely absent, in regions not in the line of sight (LOS) of the base station antenna.

The most straightforward solution for reducing these effects is increasing the number of base stations. However, this would result in an undesired increase in the network complexity, in the associated cost, in the visual impact, and in the electromagnetic pollution within the covered area. A possible solution to overcome these limitations and to face the challenge of obtaining a highly-performing communication network consists of designing a Smart Electromagnetic Environment (SEE) in which the propagation environment is used to enhance the properties of the wireless system itself. In this view, the environment is no longer a “passive” part of the wireless system, affecting the propagation in an uncontrollable way but can actively contribute to improve the system’s performance (see, for example, [4–9]).

The implementation of an SEE is possible thanks to the introduction of several active and passive devices that are able to reach blind spots or to cover desired areas without increasing the number of base stations. Among them, Smart Electromagnetic Skins (SEs) [9–16], are very thin passive surfaces capable of enabling non-specular reflection to reach blind spots or cover target areas. In addition, they must also satisfy constraints such as the reduced visual/environmental impact and the low cost. More sophisticated versions of SEs are the so-called Reflecting Intelligent Surfaces (RISs), capable of dynamically changing the re-radiation direction in real-time by adjusting the surface’s behavior through the use of reconfigurable elements [17–32]. In the following, the focus will be on SEs, i.e., on entirely passive configurations. However, most of the discussed considerations are also valid for RISs.

The literature on SEs is mainly focused on their effects on the communication network more than on their design and realization. The latter remains an open issue, especially considering the low cost and the reduced visual impact requirements [5].

Usually, SEs are assumed to be planar surfaces integrated into building’ walls [9–16]. However, this solution is not always feasible for the specific orientation of the building with respect to the base station, for buildings with plenty of windows, and for architectural heritage-restricted buildings in historical city centers [33]. Thus, other supporting structures must be used. Here, the possibility of integrating a smart skin in a street light or a traffic light pole is investigated. While such a solution is mentioned in [5], to the best of the authors’ knowledge, this is the first time that an analysis of its performance and its use in a real scenario is presented. The advantages of such a configuration are several. Since the supporting structures belong to the urban furniture, the SE installation is subject to fewer limitations. The SE can be rotated on the pole to maximize the link with the base station. The field re-radiated by the SE is not affected by the contribution of the wall, which could be not negligible [34]. Finally, several SEs, with different orientations, can be mounted on the same pole to cover different areas, with the incident signal arriving from the same direction, or to redirect in the same area the field radiated by different base stations.

In principle, a planar SE can also be integrated into the urban furniture. However, as discussed in Section 4.1, this may not represent the optimal solution, especially when aiming to maintain a limited volume for the structure. The alternative presented here consists of using a curved SE, that can be easily located between the supporting pole and a concentric radome. In the following, the main aspects of the curved SE design are discussed and compared with a planar surface that occupies the same volume. Numerical results show that the curved solution is feasible and that it guarantees even better performance than the planar one. Since the SE is assumed to be manufactured with square patches printed on a grounded dielectric layer, its cost is comparable with that of a planar solution. The choice of the substrate material and its thickness is dictated by its possibility to be easily bent. Moreover, it is worth noting that only a single cylindrical curvature is required which is not expensive to obtain. Finally, the curvature of the SE allows its placement under a cylindrical radome, which is low cost in comparison with a shaped radome that would be required if a planar SE with comparable performance is used, as discussed in Section 4.1.

The paper is organized as follows. In Section 2, the reference scenario is introduced, while in Section 3, the main aspects taken into account during the curved SES design are discussed. Finally, in Section 4, several numerical results are presented, such as those related to the comparison between the performance of the curved SES and a planar one occupying the same volume. Then, the effect of the radome is analyzed, and to conclude, the coverage provided by the SES in the scenario introduced in Section 2 is shown. All these results confirm the feasibility of curved smart electromagnetic skins and confirm that their performance is never lower but, in some cases, even better than a planar solution with the same visual impact and comparable cost.

2. Scenario

Figure 1 represents a typical application scenario where curved SESs, operating in the 5G Italian millimeter band 26.5–27.5 GHz, could be usefully exploited to increase the coverage of crowded areas. It consists of a neighborhood square that hosts goods, fruit, and vegetable market in the morning, and some recreational events at night, especially in the summertime. The square also hosts and is surrounded by numerous shops, restaurants, pizzerias, and pubs, several of them with outdoor tables.

We assume that a base station (BS) located on a border of the square (red dot in Figure 1) at a height of 6.3 m provides the 5G service in the millimeter band. It is supposed to consist of a 16×16 Multiple In Multiple Out (MIMO) array that can cover a horizontal angular area of $\pm 60^\circ$ [35].

In the square, several light poles (yellow dots in Figure 1) in the line of sight of the base station are already present and they can allocate an SES. In particular, the SES can be positioned at 6.3 m from the road surface, inside a cylindrical radome conformal with the pole itself, as represented in Figure 2.

Typical diameters of street light poles vary from 98 mm to 240 mm, depending on their height and the considered position of SES along the pole itself. In the following, the pole diameter of 240 mm, representing the worst case, can be considered, while it will be assumed that the SES is encapsulated within a cylindrical radome whose diameter is $D_r = 300$ mm at maximum.



Figure 1. A possible scenario of application 5G. The yellow area is the LOS area covered by the base station (BS), represented by a red dot. The hatched red area represents the market area. The yellow-red circled dots identify the location of existing light poles where curved SESs can be mounted.



Figure 2. Light pole supporting a curved SES located in a cylindrical radome.

3. Design of a Curved SES

Figure 3 shows the geometry of the considered curved SES and the adopted reference system. It is worth noting that the SES is located between the pole and the radome, but it is not concentric to them. In this way, the curved SES has a minimum curvature radius of 175 mm, which is slightly larger than the radius of the pole. In this case, the aperture angle of the curved SES in the horizontal plane is 96° . The equivalent planar area of the SES measures $300\text{ mm} \times 340\text{ mm}$, which corresponds to about $27.5\lambda_0 \times 31\lambda_0$, where λ_0 is the free space wavelength at the upper bound of the considered frequency band (i.e., 27.5 GHz).

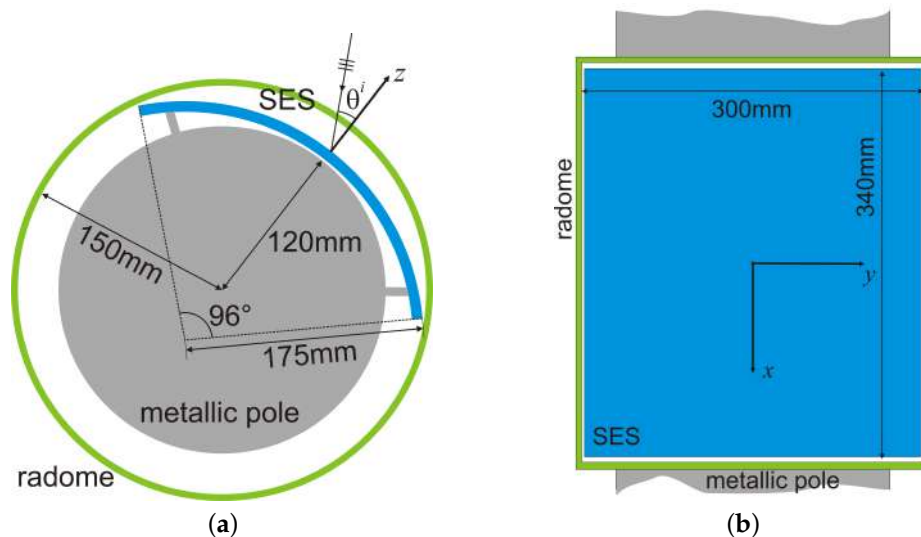


Figure 3. Top (a) and lateral (b) view of the considered geometry, with the adopted coordinate reference system.

When a planar SES is mounted on the wall of a building, the incident angle remains the same for all the unit cells; it depends on the relative position of the base station and the wall itself and cannot be changed. Vice versa, if the SES is mounted on a pole, it is possible to arrange its orientation so that the incident angle is not too skewed. In the case of the curved configuration, the angle of incidence on each re-radiating element depends on its position in the surface layout. Moreover, it depends on the SES curvature and its

variation along the SES is minimum when the field impinges orthogonally on the SES central element (i.e., when $\theta^i = 0$, with θ^i defined in Figure 3). For the case considered here, this condition implies having a maximum angle of incidence equal to 47° . Thus, if the plane wave impinges on the central element with an angle θ^i different from zero, the maximum angle of incidence on the elements will increase by θ^i .

As a re-radiating element, a simple square patch has been selected since the aim is to demonstrate the profitable utility of a curved SES for 5G applications. Although simple, the square patch allows its use with double polarization and good performance in the 5G frequency band allocated in Europe (i.e., 26.5–27.5 GHz).

Each re-radiating element has a dimension of $5.45 \text{ mm} \times 5.45 \text{ mm}$ (i.e., $\lambda_0/2 \times \lambda_0/2$ at 27.5 GHz) and is made of a square metallic patch of side W , as shown in the inset of Figure 4, printed on a grounded dielectric DiClad527 substrate ($\epsilon_r = 2.55$, $\tan \delta = 0.0022$), $h = 0.8 \text{ mm}$ thick. Thus, the SES layout consists of 55×62 cells. The choice of the substrate thickness is guided by the necessity to have a surface that can be curved, once the re-radiated elements are printed.

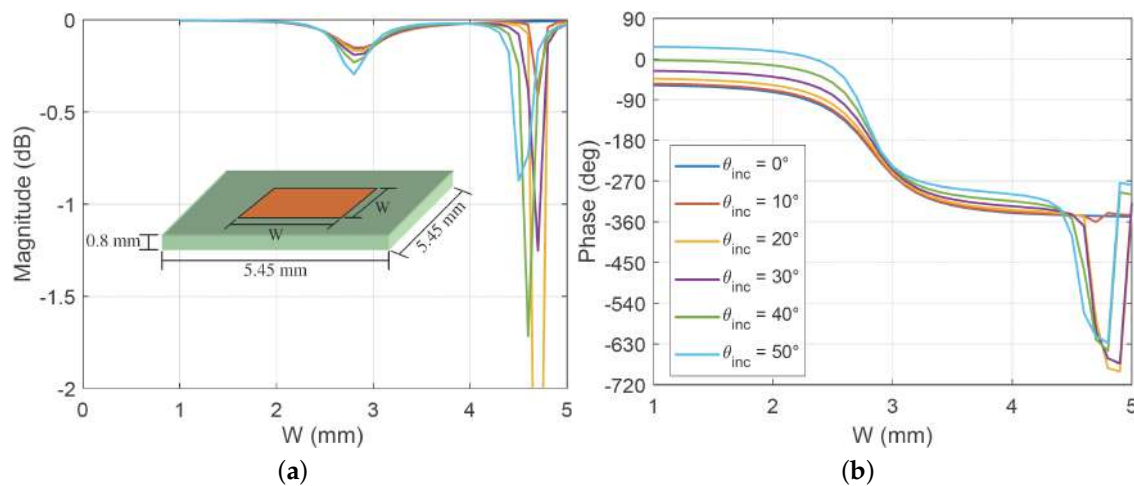


Figure 4. Magnitude (a) and phase (b) of the reflection coefficient versus the patch size at 27 GHz for different plane wave incidence angles when the element is embedded in a periodic lattice with period $5.45 \text{ mm} \times 5.45 \text{ mm}$.

Figure 4 shows the magnitude (a) and phase (b) of the reflection coefficient versus the patch size W , evaluated at 27 GHz for different plane wave incidence angles when the element is assumed embedded in a periodic lattice. Since the curvature radius is 15λ at 26 GHz, it does not significantly affect the phase of the reflection coefficient provided by the unit cell. For this reason, its analysis has been carried out considering it is embedded in an infinite periodic array. This statement is supported by Figure 5, where the variation of the phase of the reflection coefficient evaluated with three different methods is plotted: using the planar infinite periodic model, considering a finite 5×5 element planar array and a finite 5×5 element array concentric to a cylinder with radius of curvature equal to 15λ , sketched in the inset of Figure 5. The agreement among the curves plotted in the figure, confirms that the three approaches provide essentially the same results and therefore each of them could be equally used.

The plots in Figure 4 highlight the existence of a deep resonance for $W \sim 4.6 \text{ mm}$ for angles of incidence greater than zero. The presence of this resonance limits to $W = 4 \text{ mm}$ the maximum size of the patch. Moreover, for values of W lower than 1 mm the phase of the reflection coefficient stays almost constant, and therefore the lower bound of the range of variation for the patch size is set to 1 mm. As expected, the re-radiating element does not cover a phase range of 360° , but it introduces a variation of almost 290° ; this implies that the required phase delay is approximated at certain points on the surface, leading to a subsequent reduction in the performance of the SES. However, as already pointed out, here

we aim to prove the feasibility of a curved SES and compare its performance with those of a planar one, designed using the same unit cell. The optimization of the unit cell will be an object of future analyses.

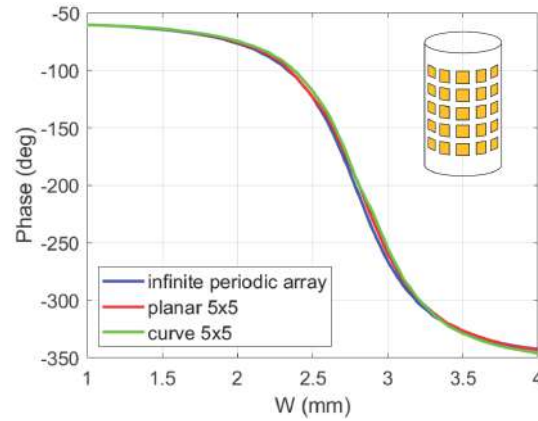


Figure 5. Phase of the reflection coefficient for the unit cell evaluated with three different models. Inset: sketch of the 5×5 array conformal to a cylinder with a radius of curvature equal to 15λ .

Assume that $f(u, v)$ is the desired phase distribution on a plane uv orthogonal to an arbitrary unit vector \hat{k} . In the case of uniform aperture distribution \hat{k} is the direction of maximum radiation. With reference to Figure 6, \hat{k}' denotes the direction of incidence of the impinging plane wave, while \vec{r}'_{ij} identifies the center of the ij -th SES re-radiating element. Hence, the phase delay $\Delta\phi_{ij}$ that the ij -th element has to introduce is

$$\Delta\phi_{ij} = k_0\hat{k}' \cdot \vec{r}'_{ij} - k_0\hat{k} \cdot \vec{r}'_{ij} + f(u_i, v_j) + \phi_0, \tag{1}$$

where $f(u_i, v_j)$ is the phase distribution corresponding to the ij -th element projected on the plane uv , and ϕ_0 is an arbitrary constant phase.

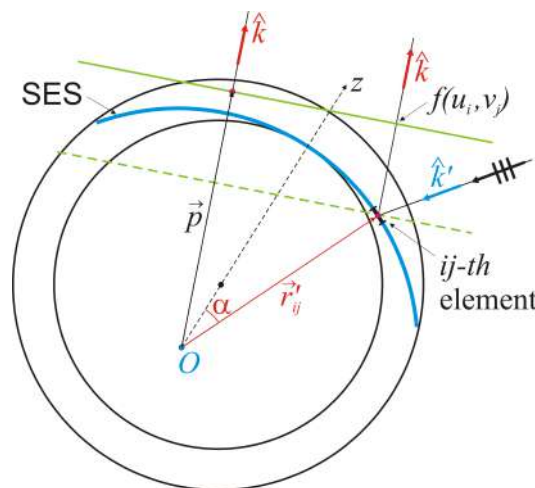


Figure 6. Geometry of the problem.

Figure 7a shows the phase delay introduced by each element of the SES in case of an incidence $\theta^i = 10^\circ$, $\phi^i = -90^\circ$ and required uniform phase distribution on a plane orthogonal to the direction $\theta^o = 30^\circ$, $\phi^o = 70^\circ$: note that the orientation of the SES is selected to have θ^i close to its optimal value, according to the previous discussion. Figure 7b shows the phase delay map for the generation of the cosecant squared pattern that will be described in Section 4.4.

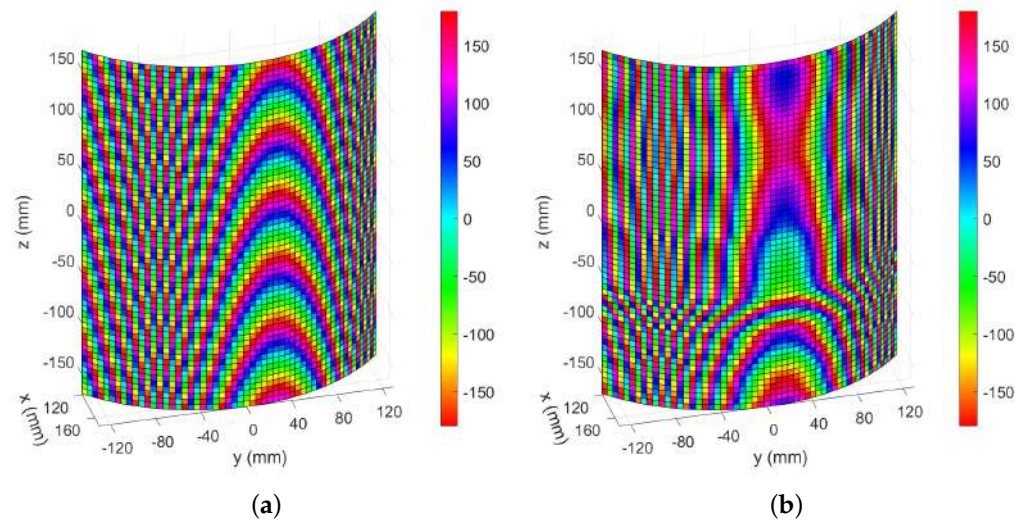


Figure 7. Phase delay maps that generate (a) a pencil beam in the direction $\theta^o = 30^\circ$, $\phi^o = 70^\circ$ in case of an incidence $\theta^i = 10^\circ$, $\phi^i = -90^\circ$, and (b) a cosecant squared pattern in the vertical plane rotated clockwise of 30° with respect to the z -axis of the SES shown in Figure 3 when $\theta^i = 20^\circ$, $\phi^i = 90^\circ$.

4. Results

In this section, some numerical results, obtained with CST Microwave Studio [36], are presented. They aim to confirm the curved SES feasibility and its possible application in a real scenario.

4.1. Comparison between Planar and Curved SES

The performance of the curved SES is compared with that of two planar configurations, having the same height as the curved one, but different widths. Figure 8 shows with the same scale the cross-section of the pole with the three SES (the curved one and the two planar) and the radome needed for their protection and camouflaging. The first considered planar SES (Figure 8b) is tangent to the pole and fits the space between the pole and the radome, thus its width is equal to 180 mm and it is discretized with 33 unit cells. In the second case (Figure 8c), the planar SES has a width of 262 mm, which is the length of the curved SES chord and it is discretized with 48 unit cells. The latter case will be considered only for reference since its installation is not feasible. In fact, if the entire structure volume is to be held, the pole would be cut to accommodate the surface inside the radome and this is not clearly possible. On the contrary, if the SES is mounted on the pole as it is, it would be necessary to manufacture a customized radome, with a significant increase in the cost, the volume, and, therefore, in the visual impact as it appears from Figure 8c.

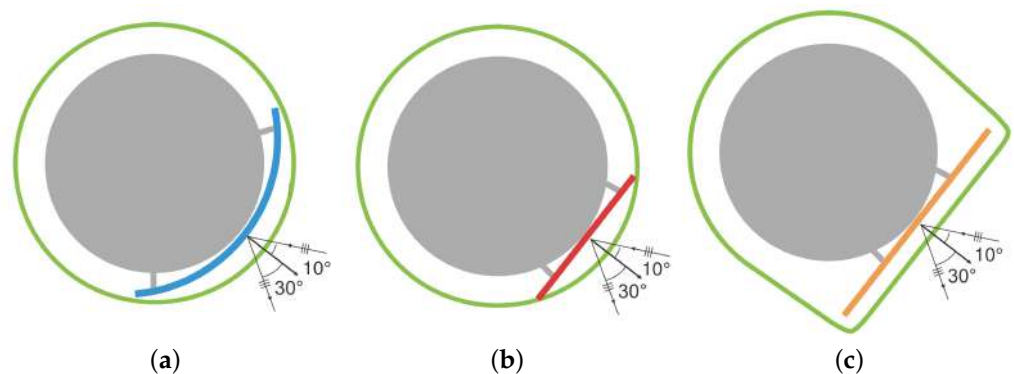


Figure 8. Cross sections of (a) the proposed curved SES, (b) a flat SES that can be allocated into a cylindrical radome with a diameter of 30 cm, (c) a flat SES with a horizontal dimension equal to the length of the curved SES chord that requires a customized radome.

In Figure 9, the 2D map of the Radar Cross Section (RCS) [37] evaluated at 27.0 GHz for the curved SES is plotted. As it appears, the SES collimates the beam in the desired direction, the side lobes are mainly present in the two principal planes, while out of them the RCS value is strongly lower.

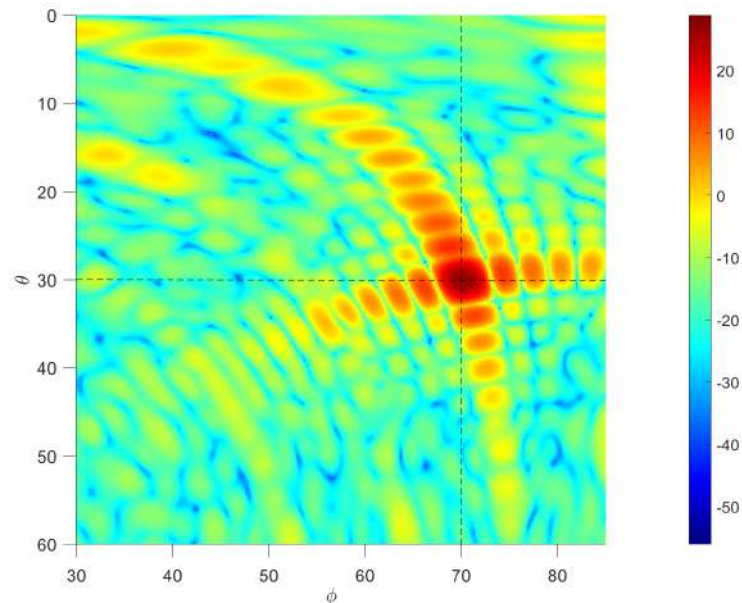


Figure 9. 2D map of the RCS of the curved SES evaluated at 27.0 GHz when a plane wave impinges from $\theta^i = 10^\circ$, $\phi^i = -90^\circ$.

In Figure 10, the RCS in the vertical (left) and horizontal (right) planes with respect to the ground, evaluated for both the curved and the narrower flat SES at 26.5 GHz (Figure 10a,b), 27 GHz (Figure 10c,d), and 27.5 GHz (Figure 10e,f) are shown. It is important to highlight that in Figure 10, $\theta' = 0^\circ$ corresponds to the nominal beam pointing direction $\theta^o = 30^\circ$, $\phi^o = 70^\circ$. For the sake of readability, the patterns for the larger SES are omitted, since they are higher but very similar to those of the smaller SES. Despite the curvature, which reduces the effective area of the surface and tends to spread the incident field, the plots confirm that the curved solution outperforms the planar one, keeping the occupied volume equal. In the vertical plane, the RCS diagram for the curved configuration is almost the same as that for the planar case, a part for a shift due to the higher maximum value of its RCS. In the horizontal plane, the pattern radiated by the curved SES is less symmetrical, especially at 27.5 GHz, where the side lobes increase with respect to those of the planar one, still maintaining a sufficiently low level. The good performance of the curved SES is also confirmed by Figure 11a, where the frequency behavior of the maximum RCS is plotted for the three considered smart surfaces. As predictable from the plots in Figure 10, the maximum value of the RCS obtained with the curved SES is never lower than that of the narrower planar configuration, while at the central frequency, it is higher by approximately 3 dB. As expected, the maximum RCS of the curved SES is lower than that of the larger planar (theoretical) solution, but the difference between the value of the provided maximum RCS is less than 1 dB at the central frequency. Finally, it is worth noting that within the considered frequency band indicated in the plot for the sake of clearness, the variation of the maximum RCS is lower than 1 dB for the curved SES.

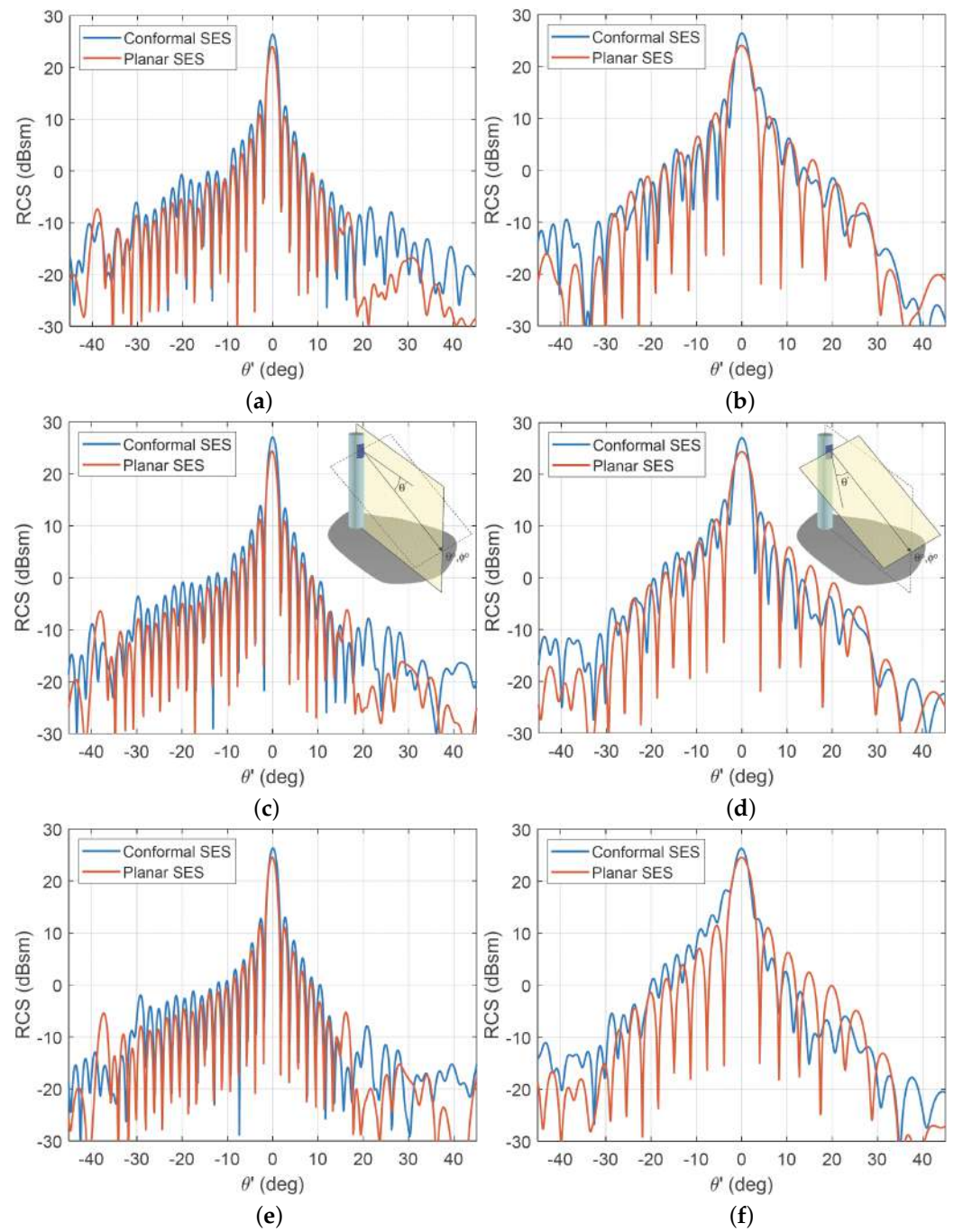


Figure 10. Comparison between the simulated RCS for a vertical polarization of the field in the vertical (left) and horizontal (right) planes, for the curved and the narrower planar SESs (i.e., 180 mm × 340 mm) at the lower (26.5 GHz (a,b)), central (27.0 GHz (c,d)) and upper (27.5 GHz (e,f)) frequencies when a plane wave impinges on the SES from $\theta^i = 10^\circ$, $\phi^i = -90^\circ$. $\theta' = 0^\circ$ corresponds to the nominal beam pointing direction $\theta^o = 30^\circ$, $\phi^o = 70^\circ$.

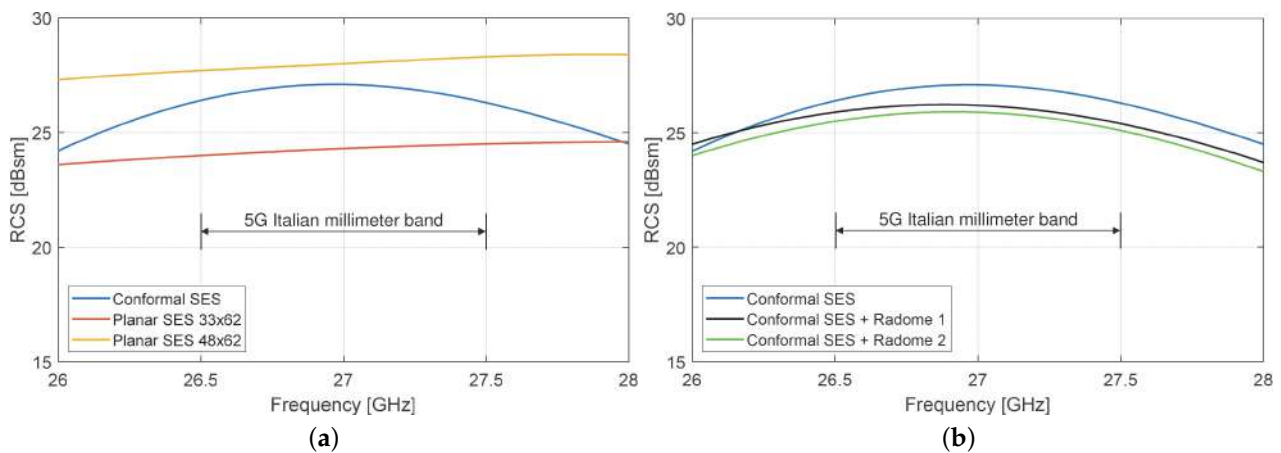


Figure 11. Maximum RCS value versus frequency: (a) comparison between curved and planar SESs in the absence of any radome; (b) influence of the radome for the curved SES.

4.2. Radome Influence

To assess the impact of the radome on the curved SES, the effect of two possible cylindrical structures, concentric to the pole and with an internal radius of 150 mm, has been investigated. The first is made of a PTFE layer ($\epsilon_r = 2$, $\tan \delta = 0.0002$) 3.85 mm thick. The second is made of LEXANTM ($\epsilon_r = 2.8$, $\tan \delta = 0.01$) and has a thickness of 3.26 mm. For both radomes, the layer thickness corresponds to a quarter of the wavelength in the dielectric. The obtained RCS patterns, which are not shown for the sake of compactness, are very similar to those shown in Figure 10, but slightly lower. To appreciate the RCS lowering, Figure 11b compares the maximum RCS obtained when the two radomes are present with the case they are absent. It is worth noting that the PTFE radome decreases the RCS at 27 GHz by about 0.9 dB, while the LEXANTM one, characterized by higher losses, by about 1.2 dB.

4.3. Incidence Sensitivity

To determine the necessary accuracy for fixing the SES to the pole, we analyzed how the RCS is modified by a rotation of the SES around the pole or by its vertical translation. It is worth noting that since the base station is fixed a vertical translation of the SES corresponds to a change in the incidence angle of the impinging wave in the vertical plane. In particular, we considered the curved SES designed in the previous section to redirect a plane wave arriving from a direction characterized by $\theta_i = 10^\circ$ and $\phi_i = -90^\circ$, and we separately changed the angles of incidence to see how this affects the SES performance. The RCS obtained by changing the incident angle in the vertical plane of $\pm 3^\circ$ is plotted in Figure 12a, while in Figure 12b the effect on the RCS when the SES is rotated along the pole axis (i.e., the x axis) is shown. As expected, a variation of the angle of incidence corresponds to a deviation in the pointing direction in both cases. Specifically, as it appears from the plots in Figure 12, the increase in the incident angle corresponds to a decrease in the pointing angle and vice versa. Hence, it enables slight adjustment of the antenna coverage during installation by rotating the SES on the pole or making vertical translations. Moreover, in the vertical plane, a slight reduction in the maximum RCS can be appreciated, while its diagram stays the same. Vice versa, in the other plane we can observe a distortion of the RCS diagram, which is however slight when the incidence angle varies no more than $\pm 2^\circ$.

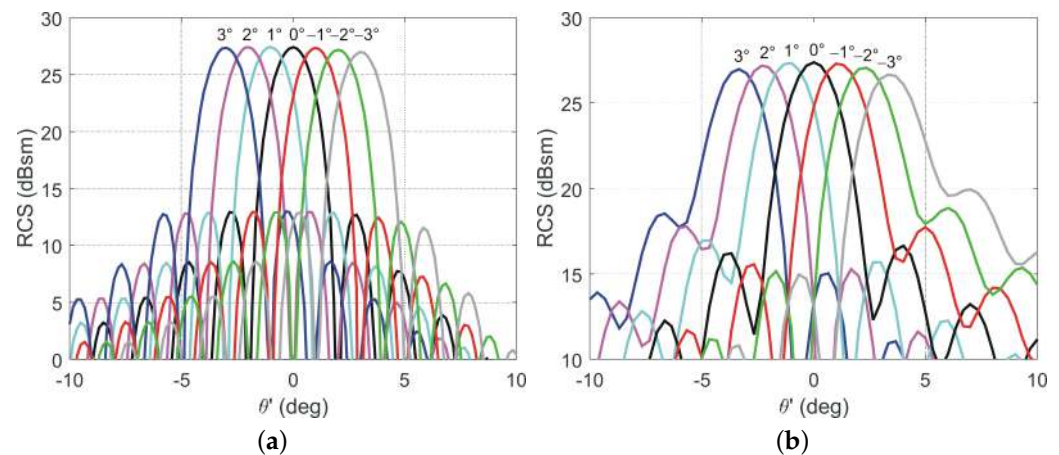


Figure 12. RCS patterns at 27 GHz: (a) in the vertical plane when the incident angle varies in the vertical plane with respect to the nominal incidence; (b) in the horizontal plane when the incident angle varies in the horizontal plane with respect to the nominal incidence.

4.4. Example of Real Application

As an example of application, the link between the base station denoted by BS in Figure 1 and the SES located at a distance of 45 m from it (denoted by SES in the same figure) is considered. The SES is in the far field of the base station, and therefore the field impinging on it can be modeled as a plane wave. It is assumed that both the base station and the SES are located at the same height of 6.3 m, and the direction of the plane wave incident on the SES makes an angle $\theta_i = 20^\circ$ with the unit vector orthogonal to the SES surface on its center (i.e., the z-axis in Figure 3). The SES is supposed to be used to provide coverage to the street at its left, which is not in the line of sight of the base station. It means that the SES has to focalize the incident field in a direction making 30° with respect to its z-axis (see Figure 3).

A cosecant squared beam has to be generated in the vertical plane to illuminate the street surface uniformly. To this purpose, Powell's direction set algorithm (DSA) with implicitly constrained current elements [38] has been used to synthesize the phase of the scattered field on the SES aperture. Figure 7b shows the phase delay that each element of the SES has to introduce.

The field scattered by the SES has been calculated by using CST. Figure 13 shows the simulated radar cross section in the vertical plane for the design frequency and for those limiting the considered band. A cosecant squared curve (red) is superimposed as a reference. We can observe several ripples in the patterns, including in the main lobe. They are due to the finiteness of the SES combined with the fact that a plane wave is impinging on it. As a matter of fact, differently from a classical reflector antenna where the feed illuminates the edges with reduced power (typically -11 dB with respect to the maximum), now the whole SES is uniformly illuminated. Thus, the ripples observed in the cosecant squared pattern are due to the field diffracted by the SES borders. While the variation in the ripple is acceptable for the specific application, it is worth noting that mitigating this ripple would lead to a significant increase in the vertical size of the reflecting surface and a subsequent increase in the cost of the SES. The three patterns in Figure 13 are very close to each other, and this confirms that the designed SES is suitable for the considered frequency band.

Then, the field map was georeferenced and calculated at ground level. In particular, we considered a BS characterized by a full MIMO array of dimensions $8\lambda \times 8\lambda$, with λ the free space wavelength at 27 GHz. The dimensions of the BS assure that the far-field starts at a distance less than 3 m for the frequency band of interest. Furthermore, the dimensions of the SES and its distance from the BS allow approximating the impinging spherical wave on the SES as a plane wave. In fact, the variation between the path lengths of an impinging spherical and plane wave is less than 0.0525λ .

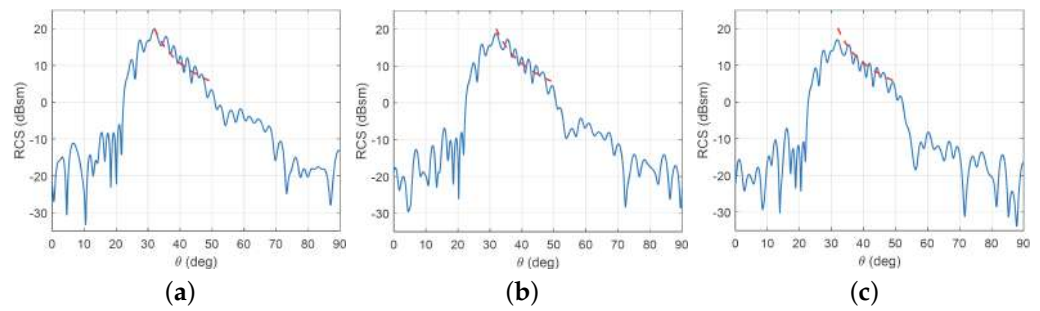


Figure 13. RCS patterns in the vertical plane $\phi = 30^\circ$: (a) 26.5 GHz; (b) 27.0 GHz; (c) 27.5 GHz. The dashed red line represents the ideal cosecant squared RCS.

Thus, the power density S^i impinging on the SES is computed as $S^i = \text{EIRP} / (4\pi\Delta_{BS-SES})$, where Δ_{BS-SES} is the distance between the BS and the SES. In the following, the effective isotropic radiation power (EIRP) is assumed equal to 1 W. Then, the power density S^s scattered at ground level is computed as $S^s = S^i \text{RCS}(\hat{R}) / (4\pi R^2)$, where the unit vector \hat{R} identifies the direction between the SES and the observation point at the ground and R its distance. Figure 14 shows the estimated power density scattered by the SES at 27 GHz: as required, the coverage of the street has been obtained. Furthermore, the field scattered by the SES is summed up to the field radiated by the BS by considering the correct phase delay introduced by the different path lengths. The total power density at ground level is shown in Figure 15. Although the power density radiated directly by the BS is about 20 dB higher than the power density scattered by the SES, the street will not be covered without the latter. Clearly, the considered SES has a limited size and therefore intercepts a small portion of the field radiated by the base station. Nevertheless, the provided power density on the street is sufficient to guarantee a stable connection. A larger SES would increase the field intensity but at the cost of a higher visual impact.

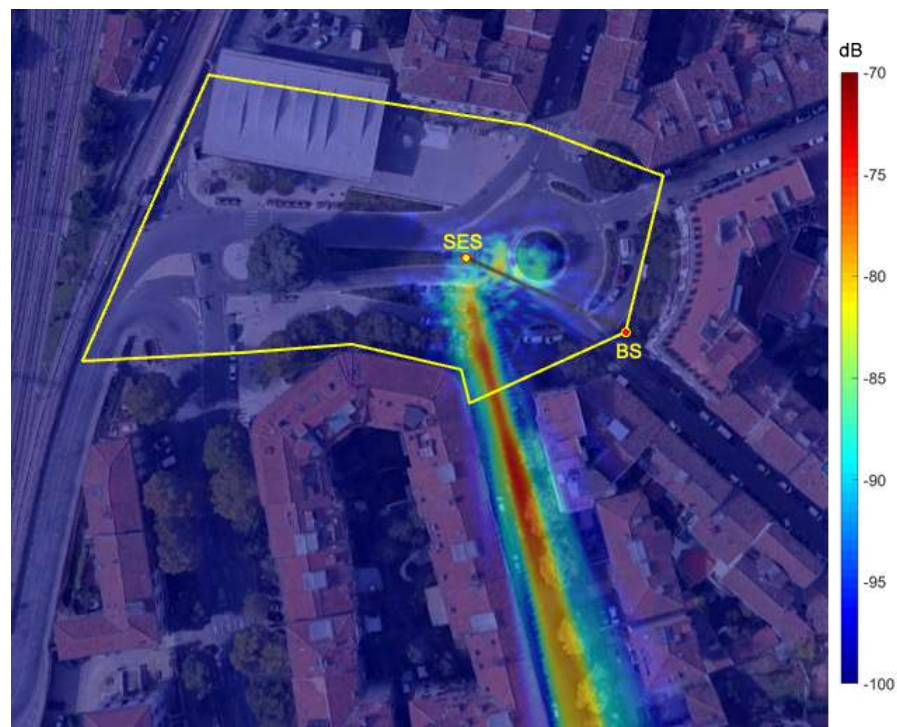


Figure 14. Map of the simulated power density scattered by the curved SES at ground level superimposed on the urban scenario.

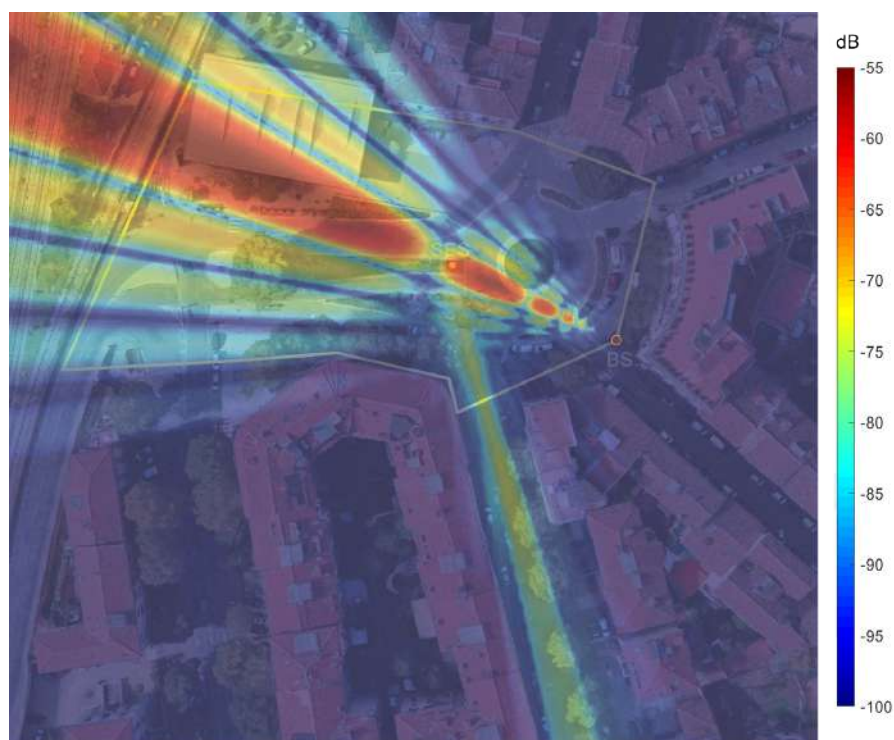


Figure 15. Map of the simulated power density radiated by the BS and scattered by the curved SES at ground level superimposed on the urban scenario.

5. Conclusions

The results presented in the paper prove that a curved smart electromagnetic skin (SES) can be conveniently integrated with a light or traffic light pole to enhance the coverage of a base station operating in the 5G Italian millimeter-wave band (26.5–27.5 GHz).

While a planar SES mounted onto buildings' walls requires a specific orientation of the building with respect to the base station and its installation is limited by architectural restrictions, the proposed curved SES can be easily installed onto any existing poles and hidden under a cylindrical radome to minimize the visual impact.

The features of a curved SES have been compared with those of a planar configuration allocable under the same cylindrical radome. This analysis has shown that the former solution performs better, with an increase in the RCS of more than 3 dB. In principle, a larger planar SES can also be adopted to obtain the same performance as the curved one. However, its use results in increased manufacturing and installation complexity and cost (a shaped radome, instead of a cylindrical one, is now necessary) with further growth of the visual impact. Therefore, the proposed curved solution represents the optimal compromise among the performance, visual impact, installation easiness, and costs.

Moreover, the proposed solution has been tested for sensitivity to positioning errors and its performances have been analyzed in a real urban scenario. The results confirm that a curved SES can be profitably used in a millimeter wave 5G wireless system to enhance its performance.

Author Contributions: Conceptualization, A.F., M.B., A.M. (Agnese Mazzinghi), A.M. (Andrea Massaccesi), and P.P.; methodology, A.F., M.B., A.M. (Agnese Mazzinghi), A.M. (Andrea Massaccesi) and P.P.; software, A.F., M.B., A.M. (Agnese Mazzinghi), A.M. (Andrea Massaccesi) and P.P.; validation, A.F., M.B., A.M. (Agnese Mazzinghi), A.M. (Andrea Massaccesi) and P.P.; formal analysis, A.F., M.B., A.M. (Agnese Mazzinghi), A.M. (Andrea Massaccesi) and P.P.; investigation, A.F., M.B., A.M. (Agnese Mazzinghi), A.M. (Andrea Massaccesi) and P.P.; resources, A.F. and P.P.; data curation, A.F., M.B., A.M. (Agnese Mazzinghi), A.M. (Andrea Massaccesi) and P.P.; writing—original draft preparation, A.F., M.B., A.M. (Agnese Mazzinghi), A.M. (Andrea Massaccesi) and P.P.; writing—review and editing, A.F., M.B., A.M. (Agnese Mazzinghi), A.M. (Andrea Massaccesi) and P.P.; project administration, A.F.

and P.P.; funding acquisition, A.F. and P.P. All authors have read and agreed to the published version of the manuscript.

Funding: This research was carried out in the framework of the Italian National Recovery and Resilience Plan (NRRP) of NextGenerationEU, partnership on “Telecommunications of the Future” (PE0000001—program “RESTART”).

Conflicts of Interest: The authors declare no conflict of interest.

Abbreviations

The following abbreviations are used in this manuscript:

SES	Smart Electromagnetic Skins
BS	Base Station
LOS	Line of Sight
RCS	Radar Cross Section

References

1. Tataria, H.; Shafi, M.; Molisch, A.F.; Dohler, M.; Sjöland, H.; Tufvesson, F. 6G Wireless Systems: Vision, Requirements, Challenges, Insights, and Opportunities. *Proc. IEEE* **2021**, *109*, 1166–1199. [\[CrossRef\]](#)
2. Chowdhury, M.Z.; Shahjalal, M.; Ahmed, S.; Jang, Y.M. 6G Wireless Communication Systems: Applications, Requirements, Technologies, Challenges, and Research Directions. *IEEE Open J. Commun. Soc.* **2020**, *1*, 957–975. [\[CrossRef\]](#)
3. Matthaiou, M.; Yurduseven, O.; Ngo, H.Q.; Morales-Jimenez, D.; Cotton, S.L.; Fusco, V.F. The Road to 6G: Ten Physical Layer Challenges for Communications Engineers. *IEEE Commun. Mag.* **2020**, *59*, 64–69. [\[CrossRef\]](#)
4. Erricolo, D.; Rozhkova, A.; Stutts, A.C. Towards Smart Electromagnetic Environments. In Proceedings of the 2021 Computing, Communications, and IoT Applications (ComComAp), Shenzhen, China, 26–28 November 2021.
5. Flamini, R.; De Donno, D.; Gambini, J.; Giuppi, F.; Mazzucco, C.; Milani, A.; Resteghini, L. Towards a Heterogeneous Smart Electromagnetic Environment for Millimeter-Wave Communications: An Industrial Viewpoint. *IEEE Trans. Antennas Propag.* **2022**, *70*, 8898–8910. [\[CrossRef\]](#)
6. Liaskos, C.; Tsioliariidou, A.; Pitsillides, A.; Ioannidis, S.; Akyildiz, I. Using any surface to realize a new paradigm for wireless communications. *Commun. ACM* **2018**, *61*, 30–33. [\[CrossRef\]](#)
7. Kamaruddin, N.A.; Mahmud, A.; Alias, M.Y.B.; Aziz, A.A.; Yaakob, S. Performance Evaluation of Reconfigurable Intelligent Surface against Distributed Antenna System at the Cell Edge. *Electronics* **2022**, *11*, 2376. [\[CrossRef\]](#)
8. Massa, A.; Benoni, A.; Da Rù, P.; Goudos, S.K.; Li, B.; Oliveri, G.; Polo, A.; Rocca, P.; Salucci, M. Designing Smart Electromagnetic Environments for Next-Generation Wireless Communications. *Telecom* **2021**, *2*, 213–221. [\[CrossRef\]](#)
9. Oliveri, G.; Zardi, F.; Rocca, P.; Salucci, M.; Massa, A. Building a Smart EM Environment-AI-Enhanced Aperiodic Micro-Scale Design of Passive EM Skins. *IEEE Trans. Antennas Propag.* **2022**, *70*, 8757–8770. [\[CrossRef\]](#)
10. Oliveri, G.; Rocca, P.; Salucci, M.; Massa, A. Holographic Smart EM Skins for Advanced Beam Power Shaping in Next Generation Wireless Environments. *IEEE J. Multiscale Multiph. Comp. Tech.* **2021**, *6*, 171–182. [\[CrossRef\]](#)
11. Rocca, P.; Da Rù, P.; Anselmi, N.; Salucci, M.; Oliveri, G.; Erricolo, D.; Massa, A. On the Design of Modular Reflecting EM Skins for Enhanced Urban Wireless Coverage. *IEEE Trans. Antennas Propag.* **2022**, *70*, 8771–8784. [\[CrossRef\]](#)
12. Oliveri, G.; Zardi, F.; Rocca, P.; Salucci, M.; Massa, A. Constrained Design of Passive Static EM Skins. *IEEE Trans. Antennas Propag.* **2023**, *71*, 1528–1538. [\[CrossRef\]](#)
13. Martinez-de-Rioja, E.; Vaquero, Á.F.; Arrebola, M.; Carrasco, E.; Encinar, J.A.; Achour, M. Passive intelligent reflecting surfaces based on reflectarray panels to enhance 5G millimeter-wave coverage. *Int. J. Microw. Wirel. Tech.* **2022**, *15*, 1–12. [\[CrossRef\]](#)
14. Oliveri, G.; Salucci, M.; Massa, A. Generalized Analysis and Unified Design of EM Skins. *IEEE Trans. Antennas Propag.* **2023**, *71*, 6579–6592. [\[CrossRef\]](#)
15. Oliveri, G.; Salucci, M.; Massa, A. Features and Potentialities of Static Passive EM Skins for NLOS Specular Wireless Links. *IEEE Trans. Antennas Propag.* **2023**, *71*, 8048–8060. [\[CrossRef\]](#)
16. Benoni, A.; Capra, F.; Salucci, M.; Massa, A. Towards Real-World Indoor Smart Electromagnetic Environments—A Large-Scale Experimental Demonstration. *IEEE Trans. Antennas Propag.* **2023**, early access. [\[CrossRef\]](#)
17. Basar, E.; Renzo, M.D.; Rosny, J.D.; Debbah, M.; Alouini, M.-S.; Zhang, R. Wireless Communications Through Reconfigurable Intelligent Surfaces. *IEEE Access* **2019**, *7*, 116753–116773. [\[CrossRef\]](#)
18. Di Renzo, M.; Zappone, A.; Debbah, M.; Alouini, M.S.; Yuen, C.; De Rosny, J.; Tretyakov, S. Smart Radio Environments Empowered by Reconfigurable Intelligent Surfaces: How It Works, State of Research, and the Road Ahead. *IEEE J. Sel. Areas Comm.* **2020**, *38*, 2450–2525. [\[CrossRef\]](#)
19. Wu, Q.; Zhang, S.; Zheng, B.; You, C.; Zhang, R. Intelligent Reflecting Surface-Aided Wireless Communications: A Tutorial. *IEEE Trans. Commun.* **2021**, *69*, 3313–3351. [\[CrossRef\]](#)
20. Zhao, J. A Survey of Intelligent Reflecting Surfaces (IRSs): Towards 6G Wireless Communication Networks. *arXiv* **2019**, arXiv:1907.04789.

21. Yurduseven, O.; Assimonis, S.D.; Matthaiou, M. Intelligent Reflecting Surfaces with Spatial Modulation: An Electromagnetic Perspective. *IEEE Open J. Comm. Soc.* **2020**, *1*, 1256–1266. [[CrossRef](#)]
22. Ptilakis, A.; Tsilipakos, O.; Liu, F.; Kossifos, K.M.; Tasolamprou, A.C.; Kwon, D.H.; Mirmoosa, M.S.; Manassis, D.; Kantartzis, N.V.; Liaskos, C.; et al. A Multi-Functional Reconfigurable Metasurface: Electromagnetic Design Accounting for Fabrication Aspects. *IEEE Trans. Antennas Propag.* **2021**, *69*, 1440–1454. [[CrossRef](#)]
23. Pérez-Adán, D.; Fresnedo, Ó.; González-Coma, J.P.; Castedo, L. Intelligent Reflective Surfaces for Wireless Networks: An Overview of Applications, Approached Issues, and Open Problems. *Electronics* **2021**, *10*, 2345. [[CrossRef](#)]
24. Liu, Y.; Liu, X.; Mu, X.; Hou, T.; Xu, J.; Di Renzo, M.; Al-Dhahir, N. Reconfigurable Intelligent Surfaces: Principles and Opportunities. *IEEE Comm. Surv. Tutorials* **2021**, *23*, 1546–1577. [[CrossRef](#)]
25. Mei, P.; Cai, Y.; Zhao, K.; Ying, Z.; Pedersen, G.F.; Lin, X.Q.; Zhang, S. On the Study of Reconfigurable Intelligent Surfaces in the Near-Field Region. *IEEE Trans. Antennas Propag.* **2022**, *70*, 8718–8728. [[CrossRef](#)]
26. Dash, S.; Psomas, C.; Krikidis, I.; Akyildiz, I.F.; Pitsillides, A. Active Control of THz Waves in Wireless Environments using Graphene-based RIS. *IEEE Trans. Antennas Propag.* **2022**, *70*, 8785–8797. [[CrossRef](#)]
27. Degli-Esposti, V.; Vitucci, E.M.; Renzo, M.D.; Tretyakov, S. Reradiation and Scattering from a Reconfigurable Intelligent Surface: A General Macroscopic Model. *IEEE Trans. Antennas Propag.* **2022**, *70*, 8691–8706. [[CrossRef](#)]
28. Sharma, T.; Chehri, A.; Fortier, P. Reconfigurable Intelligent Surfaces for 5G and beyond Wireless Communications: A Comprehensive Survey. *Energies* **2021**, *14*, 8219. [[CrossRef](#)]
29. Demmer, D.; Foglia Manzillo, F.; Gharbieh, S.; Śmierczalski, M.; D’Errico, R.; Doré, J.B.; Clemente, A. Hybrid Precoding Applied to Multi-Beam Transmitting Reconfigurable Intelligent Surfaces (T-RIS). *Electronics* **2023**, *13*, 1162. [[CrossRef](#)]
30. Liu, Y.; Dou, J.; Cui, Y.; Chen, Y.; Yang, J.; Qin, F.; Wang, Y. Reconfigurable Intelligent Surface Physical Model in Channel Modeling. *Electronics* **2022**, *11*, 2798. [[CrossRef](#)]
31. Vitucci, E.M.; Fabiani, M.; Degli-Esposti, V. Use of a Realistic Ray-Based Model for the Evaluation of Indoor RF Coverage Solutions Using Reconfigurable Intelligent Surfaces. *Electronics* **2023**, *12*, 1173. [[CrossRef](#)]
32. Dai, L.; Wang, B.; Wang, M.; Yang, X.; Tan, J.; Bi, S.; Xu, S.; Yang, F.; Chen, Z.; Di Renzo, M.; et al. Reconfigurable intelligent surface-based wireless communications: Antenna design, prototyping, and experimental results. *IEEE Access* **2020**, *8*, 45913–45923. [[CrossRef](#)]
33. Oliveri, G.; Rocca, P.; Salucci, M.; Erricolo, D.; Massa, A. Multi-Scale Single-Bit RP-EMS Synthesis for Advanced Propagation Manipulation Through System-by-Design. *IEEE Trans. Antennas Propag.* **2022**, *10*, 8809–8824. [[CrossRef](#)]
34. Vaquero, A.F.; Martínez-de-Rioja, E.; Arrebola, M.; Encinar, J.A. Study on the Effect of the Wall in the Performance of an Intelligent Reflective Surface for Providing Coverage in mm-Wave Frequencies. In Proceedings of the European Conference on Antennas and Propag. (EuCAP), Florence, Italy, 26–31 March 2023.
35. Future Access 28 Ghz Phased Array Antenna Module (PAAM). 2023. Available online: <https://mmwavetech.fujikura.jp/5g/> (accessed on 31 October 2023).
36. CST Microwave Studio. 2023. Available online: <http://www.cst.com/> (accessed on 31 October 2023).
37. Balanis, C.A. *Antenna Theory Analysis and Design*, 3rd ed.; Equation (2-120a); Wiley-Interscience a John Wiley & Sons, Inc.: Hoboken, NJ, USA, 2005.
38. Buckley, M.J. Synthesis of Shaped Beam Antenna Pattern Using Implicit Constrained Current Elements. *IEEE Trans. Antennas Propag.* **1996**, *44*, 192–197. [[CrossRef](#)]

Disclaimer/Publisher’s Note: The statements, opinions and data contained in all publications are solely those of the individual author(s) and contributor(s) and not of MDPI and/or the editor(s). MDPI and/or the editor(s) disclaim responsibility for any injury to people or property resulting from any ideas, methods, instructions or products referred to in the content.